Journal of Ceramic Processing Research. Vol. 26, No. 1, pp. 76~81 (2025)
(Received 26 September 2024, Received in revised form 24 November 2024, Accepted 19 December 2024)
https://doi.org/10.36410/jcpr.2025.26.1.76

J O U R N A L O F
Ceramic Processing Research

Structural and magnetic properties of W-type hexa-ferrite $Ba_{1-x}Sm_xMg_2Fe_{15.6}Co_{0.4}O_{27}$ ferrites

Jinsong Li[a], Siyuan Li[a], Xiubin Zhao[a] and Ailin Xia[a,*]
Advanced Ceramics Research Center, School of Materials Science and Engineering, Anhui University of Technology, Maanshan, 243032, China

Sm^{3+}-substituted W-type $Ba_{1-x}Sm_xMg_2Fe_{15.6}Co_{0.4}O_{27}$ (x=0.00 to 0.30 with steps of 0.06) ferrites were prepared by a solid-state method. The XRD results indicated that the single W-type ferrite structure can be obtained for the specimens with x≤0.18, while the impurity phases appeared for x≤0.18. The lattice parameters a and c, the cell volume (V_{cell}) and the average grain size (D_a) decrease with the increase of x. From the FE-SEM images, it can be found that all the samples exhibited a hexagonal plate shape. The saturation magnetization and the initial magnetic permeability first increased with x from 0.0 to 0.12, but then decreased with x>0.12. The coercivity kept increasing with the increase of x gradually.

Keywords: W-type ferrite, Solid-state method, Magnetic properties, Permeability.

Introduction

Hexagonal ferrite has attracted increasing attention in many technical fields due to its excellent performance. It is widely used in the fields of communication, new energy, automobiles, cloud computing, lighting, IT, home appliances, industrial automation, medical, military and so on [1-6].

Generally, magnetic ferrites can be divided into M, W, Y, X, Z and U types according to their crystalline structure [4], in which M and W types are widely studied and used. W-type hexagonal ferrite has a chemical formula of $AMe_2Fe_{16}O_{27}$ (A=Ba, Sr, Me=Fe, Mg, Zn, Co, Cu, Mn and so on). Their crystal structure can be seen as an R block and an S block stacked along the c-axis of hexagonal crystal system in the order of RSSR*S*S* [7]. R block contains three oxygen ion layers, with an A^{2+} layer in the middle layer, which is the mirror plane of crystal, and S block is another oxygen ion layers without A^{2+}, stacked as spinels. In the W-type hexaferrites, the Fe^{3+} ions exist at seven different positions, namely 12k, $4f_{VI}$, 6g, 4f, 4e, $4f_{IV}$ and 2d [8]. The space group of W-type hexaferrites is P_{63}/mmc (194). The lattice parameters a of W-type and M-type hexagonal ferrite is about 0.588 nm, while the lattice parameters c is different [9].

For a long time, many attempts have been made to improve the magnetic properties of W type ferrites in hexagonal crystal system, in which ion substitution is the most widely studied. Rare earth elements may contribute to the modification of magnetic interactions and thus improve magnetic properties [10]. Wang et al. [11] prepared Co_2W type ferrite with a chemical formula $Ba_{1-x}Sm_xCo_2Fe_{16}O_{27}$ (x=0.00, 0.05, 0.10, 0.15 and 0.20) via a solid-state reaction method. With the increasing doping amount of Sm^{3+} ions, the real (ε') and imaginary parts (ε'') of the dielectric constant also gradually increases, and the maximum value of ε'' moves towards the low frequency band. When x=0.15, the magnetic complex permeability (imaginary part) μ'' improved significantly, and the peak value was about 1.75 at 18 GHz. I. Sadiq et al. [12] prepared W type ferrite with a chemical formula $Sr_{3-x}Ce_xFe_{16}O_{27}$ (x=0.00, 0.02, 0.04, 0.06, 0.08 and 0.10) by a sol-gel method. All the samples obtained are single-phase W-type structure. With the doping of rare earth Ce^{3+} ions, both the coercivity (H_c) and the electrical resistivity increase first and then decrease, while the saturation magnetization (M_s) increases in a wavy manner. Yang et al. [13] prepared $Sr_{1-x}Pr_xZn_{0.8}Co_{1.2}Fe_{16}O_{27}$ ($0.00 \le x \le 0.40$) W-type hexagonal ferrite using a traditional ceramic technology. With the increase of x, the M_s, the residual magnetization (M_r) and the magneton number (n_B) first increase for x from 0.00 to 0.16, and then decrease for x higher than 0.16. F. Aen et al. [14] synthesized Co_2W type ferrite $Ba_{1-x}Ho_xCo_2Fe_{16}O_{27}$ by a sol-gel method. They found that the grain size decreased from 44 nm to 34 nm with increasing Ho^{3+} concentration, accompanying with the decrease of dielectric constant and loss angle.

In summary, the substitution of rare earth elements significantly improves the magnetic properties. The substitution of Sm^{3+} is expected to reduce the dielectric constant and enhance the magnetic permeability. There-

*Corresponding author:
Tel/Fax: +86 05552311570
E-mail: alxia@126.com

fore, in this study, the W-type $Ba_{1-x}Sm_xMg_2Fe_{15.6}Co_{0.4}O_{27}$ (x=0.00, 0.06, 0.12, 0.18, 0.24 and 0.30) magnetic powders were prepared by a solid-state method. The effects of the Sm^{3+} content (x) on their structure and the magnetic properties are systematically studied.

Experimental Procedures

Materials

The raw materials used in this experiment were as follows: Fe_2O_3 (99.2% purity), $BaCO_3$ (99.5% purity), Sm_2O_3 (99.9% purity), MgO (99% purity) and CoO (99% purity) powders etc. All selected materials were analytical purity, no further purification treatment was required.

Preparation of W-type ferrites $Ba_{1-x}Sm_xMg_2Fe_{15.6}Co_{0.4}O_{27}$ powders

The solid-state method was used for preparation, and the approximate process was as follows: the ingredients are prepared according to the molar percentage of the main formula, and the ball: material: water ratio is 4:1:1 by mass, and milled for 2 hours using a ball mill; After ball milling, the slurry was taken out and dried in a vacuum drying oven, crushed into small pieces, and then calcined in air at 1300 °C for 2 hours in a muffle furnace. Then, used a vibrator to crush the calcined block and prepare sample powder through a 100 mesh sieve. Add 10% mass fraction PVA solution for granulation and pass through 60 mesh and 150 mesh sieves respectively to obtain qualified materials with particle sizes ranging from 150 to 60 mesh. Pressed into a circular sample (inner diameter 22 mm, outer diameter 7 mm, thickness 5 mm) under a pressure of 100 MPa. Finally, the ring sample was sintered in air at 1200 °C for 2 hours to obtain the final test sample.

Characterization

A Philips X'Pert MPD diffractometer was used to identify the phase composition of specimens (CuK_α radiation, λ=1.5406 Å). The morphology of all samples was obtained by a field emission scanning electron microscope (FESEM, Hitachi S-4800). A vibrating sample Magnetometer (VSM, MicroSense EZ7) was used to measure the room-temperature (RT) magnetic properties, and the maximum external electric field is

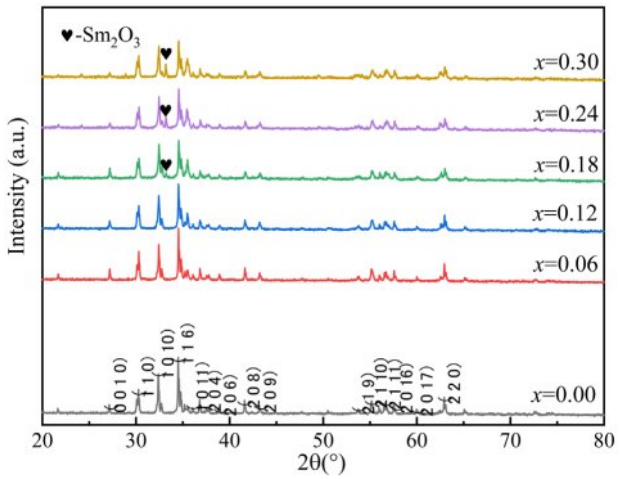

Fig. 1. The XRD results of W-type $Ba_{1-x}Sm_xMg_2Fe_{15.6}Co_{0.4}O_{27}$ ferrites.

20000 Oe. An Agilent 4284A LCR meter was used to measure the magnetic permeability of specimens at a frequency of 1MHz at room temperature.

Results and Discussion

Structure and morphology

Fig. 1 shows the XRD patterns of W-type ferrites $Ba_{1-x}Sm_xMg_2Fe_{15.6}Co_{0.4}O_{27}$ (x=0.00, 0.06, 0.12, 0.18, 0.24 and 0.30) powders. Comparing all the peaks in Fig. 1 with standard card (JCPDS PDF#75-0406), impurity peaks from Sm_2O_3 emerged for the specimens with x≥0.18. When x<0.18, no impurity peak can be found in the XRD patterns, indicating the single W-type hexagonal structure of specimens. Therefore, Sm^{3+} ions were completely dissolved in the crystalline lattice for the specimens with x<0.18. The magnetic properties of the specimen may be affected by the second phase Sm_2O_3.

The lattice parameters a and c of specimens were calculated according to the characteristic peaks (116) and (1010) by the following formula [15, 16]:

$$d_{hkl} = \left(\frac{4}{3}\cdot\frac{h^2+hk+k^2}{a^2}+\frac{l^2}{c^2}\right)^{-\frac{1}{2}} \quad (1)$$

$$V_{cell} = a^2 c \sin 120^\circ \quad (2)$$

Table 1. Different parameters calculated for all specimens.

Sm (x)	a (Å)	c (Å)	c/a	$d_{X\text{-}ray}$ (g/cm^3)	V_{cel} (Å^3)	D (nm)
0.00	5.9060	32.9152	5.5732	5.0482	994.263	53.77
0.06	5.8990	32.8162	5.5630	5.0822	988.9241	44.71
0.12	5.8998	32.8068	5.5607	5.0848	988.9090	41.13
0.18	5.8965	32.7857	5.5602	5.0966	987.1677	35.17
0.24	5.8962	32.7742	5.5585	5.1016	986.7211	33.72
0.30	5.8992	32.7703	5.5550	5.0995	987.6079	31.52

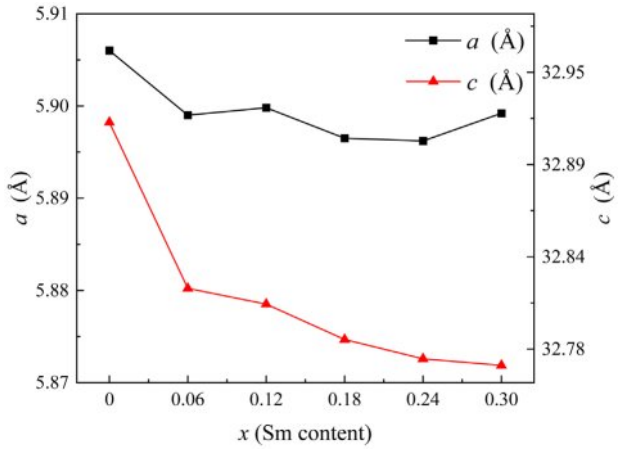

Fig. 2. The change of lattice constants *a* and *c* of specimens with different *x* from 0.00 to 0.30.

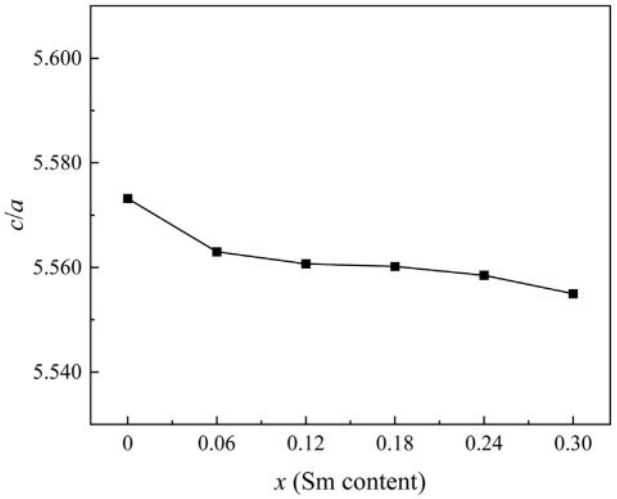

Fig. 3. The change *c/a* of specimens with different *x* from 0.00 to 0.30.

where (*h*, *k*, *l*), d_{hkl} and V_{cell} are the Miller indices, the crystal face spacing and the cell volume, respectively. The X-ray density ($d_{X\text{-ray}}$) and the average grain size (*D*) are obtained by the following two equations [17, 18]:

$$d_{X-ray} = \frac{2M}{N_A V_{cell}} \tag{3}$$

$$D = \frac{K\lambda}{\beta \cos\theta} \tag{4}$$

Here, *M*, N_A, *K*, λ, β and θ are the molar mass, 6.02×10^{23}, 0.89, 1.5406 Å, the full-width at half-

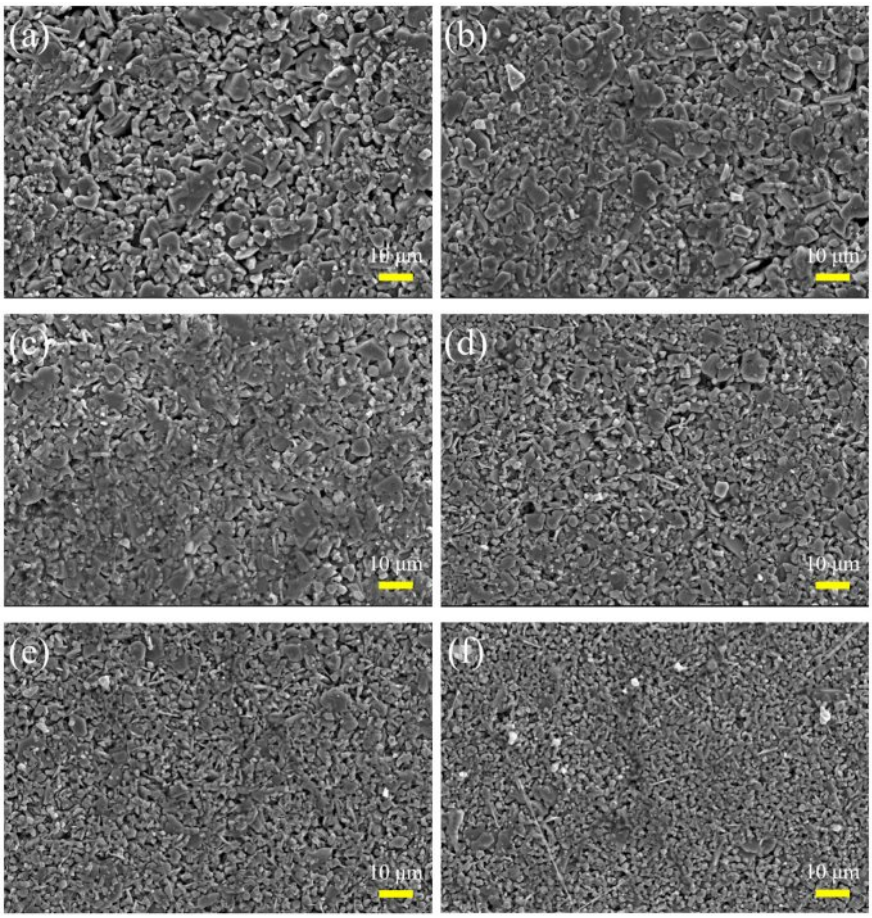

Fig. 4. Typical SEM images of $Ba_{1-x}Sm_xMg_2Fe_{15.6}Co_{0.4}O_{27}$ specimens with different *x*. (a-f): *x* is from 0.00 to 0.30 with steps of 0.06, respectively.

maximum and the Bragg diffraction angle, respectively. All the values calculated using the above four formulas are listed in Table 1.

Fig. 2 shows the change of lattice constants *a* and *c* of specimens. The *a* changes slightly. However, the *c* decreases significantly from 32.9152 Å (*x*=0.00) to 32.7703 Å (*x*=0.30). As is known, the ionic radius of Ba^{2+} and Sm^{3+} are 1.35 Å and 1.05 Å [13, 19], respectively. Therefore, when Sm^{3+} replaces Ba^{2+}, the distance between crystal planes decreases and the lattice volume shrinks. It is consistent with the changes in lattice parameters caused by ion substitution reported in early literature [20-23]. The *c* has a significant change compared to the *a* because the *c*-axis is the easy magnetized axis in W-type hexagonal ferrite [19]. The anomalous increase in V_{cel} when *x* is 0.3 may be due to the excessive addition of Sm^{3+}, which leads to an increase in the lattice constant *a*. The ratio *c/a* listed in Table 1 is between 5.5572 and 5.5630. As shown in Fig. 3, with the increase of *x*, the change in *c/a* ratio is not significant.

The typical SEM images of $Ba_{1-x}Sm_xMg_2Fe_{15.6}Co_{0.4}O_{27}$ (*x*=0.00, 0.06, 0.12, 0.18, 0.24 and 0.30) are shown in Fig. 4. All the specimens exhibit a hexagonal plate shape.The particle size decreases with the increase of *x*, which may be attributed to the deposition of Sm^{3+} on the grain boundaries [11].

Magnetic properties

Figure 5 shows the RT magnetic hysteresis loops of specimens. Under a magnetic field of 20 kOe, the hysteresis loops of the specimens approach saturation. The values of M_s, H_c, remanent magnetization (M_r) and square ratio (M_r/M_s) were obtained through the RT hysteresis loops and listed in Table 2.

Typical hysteresis loops of W-type ferrite $Ba_{1-x}Sm_xMg_2Fe_{15.6}Co_{0.4}O_{27}$ specimens (*x*=0.0~0.30) are shown in Fig. 5. The saturation magnetization (M_s) and coercivity (H_c) of magnetic powders with different Sm^{3+} concentrations (*x*) can be determined from the hysteresis loops, as shown in Table 2. From Fig. 6, it can be seen that when *x*=0.12, the peak value of M_s reaches 55.566 emu/g, which enhanced the M_s compared with the unsubstituted specimen (*x*=0). However, when *x*>0.12, the M_s decreases with the increase of *x*. The M_s of ferrite is mainly influenced by the chemical composition and the crystal structure. When *x*≤0.12, the

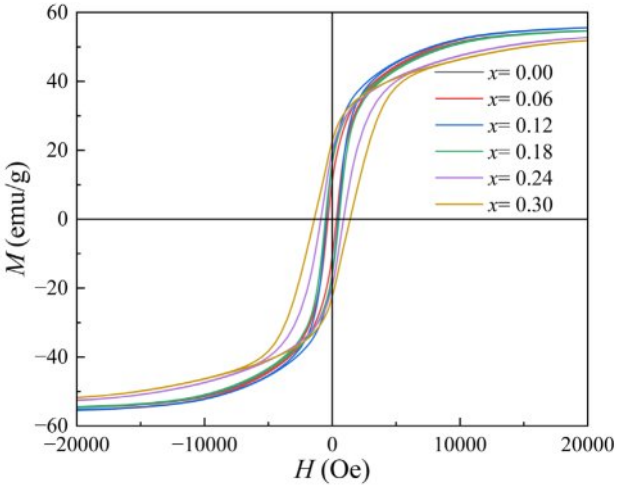

Fig. 5. RT magnetic hysteresis loops of $Ba_{1-x}Sm_xMg_2Fe_{15.6}Co_{0.4}O_{27}$ specimens with different *x*.

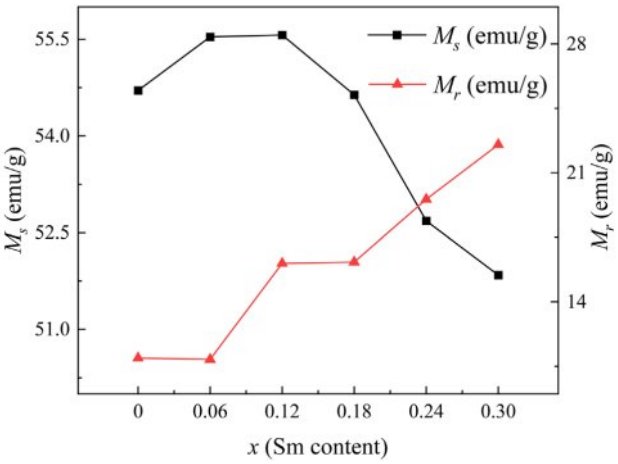

Fig. 6. The variation of M_s and M_r of $Ba_{1-x}Sm_xMg_2Fe_{15.6}Co_{0.4}O_{27}$ specimens with different *x*.

M_s increases with the increase of *x* since the trivalent Sm^{3+} replaces the divalent Ba^{2+}. In order to achieve the electronic balance, some Fe^{3+} ions in the ferrite structure will be converted into Fe^{2+} ions [24]. The migration of electrons enhances the electron leaps between the iron ions at the octahedral positions in the lattice, resulting in an enhanced hyperfinement field at the 12k position in the lattice, which strengthens the superexchange

Table 2. Magnetic properties of specimens with different Sm content (*x*).

Sm (*x*)	M_s (emu/g)	M_r (emu/g)	M_r/M_s	H_c (Oe)	μ_i
0.00	54.705	10.952	0.200	334.5	8.65
0.06	55.537	10.872	0.196	333.0	8.73
0.12	55.566	16.084	0.289	456.9	9.13
0.18	54.637	16.154	0.296	527.6	8.97
0.24	52.682	19.557	0.371	883.5	8.83
0.30	51.842	22.531	0.435	1401.9	8.64

interaction between Fe^{3+}-O-Fe^{3+} [25]. As a result, the superexchange between Fe^{3+}-O-Fe^{3+} decreases, which leads to the increase of the M_s . When x>0.12, the M_s decreases with x mainly because too much Sm^{3+} entered into the crystalline lattice, which can cause the decrease of M_s due to the weakening the superexchange between Fe^{3+}-O-Fe^{3+} resulting from the formation of a spin canting structure [26].

As shown in Fig. 7(a), the increase of H_c in specimens after the substitution of rare earth ion Sm can be ascribed to the following reasons. On the one hand, the greater magnetocrystalline anisotropy of specimens caused the greater energy required for the rotation of magnetic domains, that is, the greater H_c. When Sm^{3+} replaces Ba^{2+}, there will be a transition of Fe^{3+} to Fe^{2+} in the ferrite, and the appearance of strong Fe^{2+} ions anisotropy will lead to the increase of magnetocrystalline anisotropy. Therefore, the H_c will increase after the replacement of rare earth ions [27]. On the other hand, the larger grains are conducive to the formation of domain walls. In large grains, more domain walls move during magnetization, and the energy consumed by domain wall movement is less than that of domain rotation, resulting in a smaller amount of energy required for magnetization. Therefore, the H_c in specimens with larger grains is smaller, that is, the grain size is inversely proportional to the H_c. According to the microstructure in Fig. 4, the specimens after the replacement of Sm^{3+} have smaller grains, resulting in their high H_c [28].

Fig. 7(b) illustrates the initial magnetic permeability (u_i) of specimens with different x. As the x increases from 0.00 to 0.12, the u_i increases from 8.65 to 9.13. When x>0.12, the u_i decreases from 9.13 to 8.64. The main influencing factors on the u_i of ferrite are the M_s and the magnetic crystal anisotropy constant (K_1), as shown in the following equation [29]:

$$\mu_i \propto \frac{M_S^2 D}{K_1 + \lambda_S \sigma} \qquad (5)$$

Where λ_S and σ are the magnetostriction coefficient and the internal stress, respectively. Generally, the internal stress in ferrite materials is so low that the λ_S and σ can be ignored [30]. As described above, the replacing of Ba^{2+} by Sm^{3+} will result in the transition of Fe^{3+} to Fe^{2+}. The ion magnetic moment of Fe^{2+} ($4\mu_B$) is smaller than that of Fe^{3+} ($5\mu_B$) [13]. Therefore, this transition reduces the total ion magnetic moment in specimens, which reduces their u_i correspondingly.

Conclusions

Sm^{3+} substituted W-type barium ferrites $Ba_{1-x}Sm_xMg_2Fe_{15.6}Co_{0.4}O_{27}$ (x=0.00 to 0.30 with steps of 0.06) were obtained by a solid-state method. The XRD results indicate that the specimens with x<0.18 were single W-type hexagonal crystal structure. When x≥0.18, the impurities Sm_2O_3 phases emerged. As the x increases, both the lattice parameters a and c decrease, but c changes more significantly than a. When x≤0.12, the M_s increases with the increase of x, while when x>0.12, it begins to decrease. However, the H_c keeps increasing with the increase of x. The initial magnetic permeability of specimens exhibits the same variation as M_s. When x=0.12, it reaches a maximum.

CRediT Authorship Contribution Statement

Jinsong Li: Investigation, Methodology, Writing - original draft, Writing - review & editing, Funding acquisition. **Siyuan Li**: Writing - review & editing, Investigation, Formal analysis. **Xiubin Zhao**: Writing - review & editing, Investigation, Formal analysis. **Ailin Xia**: Funding acquisition, Methodology, Project administration, Supervision.

Declaration of Competing Interest

The authors declare that they have no known competing financial interests or personal relationships that could have appeared to influence the work reported

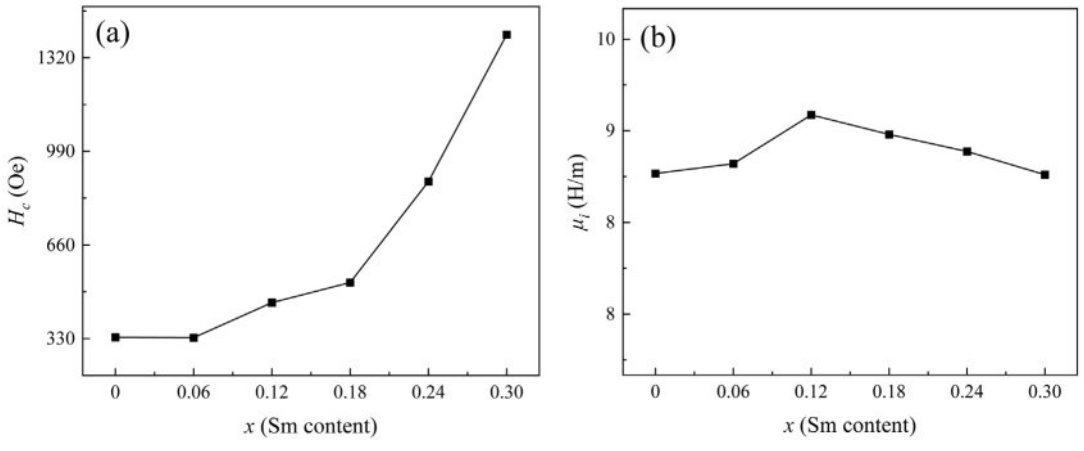

Fig. 7. The H_c (a) and the u_i (b) of specimens with different x from 0.0 to 0.3.

in this paper.

Data Availability

Data will be made available on request.

References

1. A.L. Xia, J.J. Ji, X.S. Zhu, C.C. Cao, S.B. Su, H.Y. Zhang, H.L. Li, Z.Y. Liu, and C.G. Jin, J. Mater. Sci.: Mater. Electron. 32 (2021) 12725-12731.
2. M. Etier and H. Aimomani, J. Ceram. Process. Res. 21[5] (2020) 565-570.
3. X.B. Zhao and A.L. Xia, J. Ceram. Process. Res. 24[4] (2023) 634-639.
4. Y. M. Zhang, Y.J. Yang, D.Y. Chen, C.L. Chen, and Y.T. Meng, J. Ceram. Process. Res. 24[2] (2023) 342-347.
5. X.B. Zhao, S. Zhang, J.S. Li, A.L. Xia, and Y.J. Yang, J. Ceram. Process. Res. 24[1] (2023) 98-102.
6. J.S. Li, X.B. Zhao, and A.L. Xia, J. Ceram. Process. Res. 25[2] (2024) 316-321.
7. M. Ahmad, I. Ali, and R. Grössinger, J. Alloys Compd. 579 (2013) 57-64.
8. P.S. Sawadh and D.K. Kulkarni, J. Mater. Chem. Phys. 63 (2000) 170-173.
9. Y.J. Yang, C.L. Chen, and D.Y. Chen, Magnetochemistry 8 (2022) 75.
10. J.S. Li, X.B. Zhao, and A.L. Xia, J. Ceram. Process. Res. 24[5] (2023) 894-898.
11. L.X. Wang, J. Song, Q.T. Zhang, X.G. Huang, and N.C. Xu, J. Alloys Compd. 481 (2009) 863-866.
12. I. Sadiq, I. Khan, F. Aen, M.U. Islam, and M.U. Rana, Phys. B 407 (2012) 1256-1261.
13. Y.J. Yang, X.S. Liu, and S.J. Feng, J. Ceram. Process. Res. 21[3] (2020) 378-385.
14. F. Aen, M.F. Wasiq, M.U. Rana, H.M. Khan, and M.A. Khan, J. Ceram. Int. 42[14] (2016) 16077-16083.
15. X. Niu, X. Liu, S. Feng, F. Lv, F. Huang, X. Huang, Y. Ma, and K. Huang, J. Optik 126 (2015) 5513-5516.
16. M.N. Akhtar, K. Ali, A. Umer, T. Ahmad, and M.A. Khan, Mater. Res. Bull. 101 (2018) 48-55.
17. M.J. Iqbal and S. Farooq, J. Alloys Compd. 505 (2010) 560-567.
18. Y.F. Wu, Y. Huang, and L. Niu, J. Magn. Magn. Mater. 324 (2012) 616-621.
19. F.R. Lv, X.S. Liu, and S.J. Feng, Mater. Lett. 157 (2015) 277-280.
20. I. Khan, M.N. Ashiq, I. Sadiq, A.M. Qureshi, and M.U. Rana, J. Chem. Soc. Pak. 34 (2012) 579-583.
21. M.J. Iqbal, R.A. Khan, S. Mizukami, and T. Miyazaki, Ceram. Int. 38 (2012) 4097-4103.
22. F. Leccabue, R. Panizzieri, G. Albanese, G. Leo, and N.S. Almodovar, Mater. Res. Bull. 23[2] (1988) 263-275.
23. F.K. Lotgering, P.H.G.M. Vromans, and M.A.H. Huyberts, J. Appl. Phys. 51[11] (1980) 5913-5918.
24. Y.B. Han, J. Sha, L.N. Sun, Q. Tang, Q. Lu, H.X. Jin, D.F. Jin, H. Bo, H.L. Ge, and X.Q. Wang, J. Alloys Compd. 486 (2009) 348-351.
25. J. Tang, D. Li, H. He, Y.M. Li, J.S. Zeng, and C. Liu, J. Appl. Phys. A. 126 (2020) 277.
26. M.J. Iqbal and S. Farooq, J. Mater. Res. Bull. 44 (2009) 2050-2055.
27. S. Ounnunkad, J. Solid. State. Comm. 138 (2006) 472-475.
28. D.M. Hemeda, A.A. Sharif, and O.M. Hemeda, J. Magn. Magn. Mater. 315 (2007) L1-L7.
29. H. Su, H. Zhang, X. Tang, B. Liu, and Z. Zhong, J. Alloys Compd. 475[1] (2009) 683-685.
30. Y. Peng, X.H. Wu, Z.Y. Chen, W.H. Liu, F. Wang, Z.K. Feng, Y.J. Chen, and V.C. Harris, J. Alloys Compd. 630 (2015) 48-53.